IEEE *Access*
Multidisciplinary : Rapid Review : Open Access Journal

Synthesizing Foot and Ankle Kinematic Characteristics for Lateral Collateral Ligament Injuries Detection

XIN LIU[1,2]**, CHEN ZHAO**[1,5]**, BIN ZHENG**[2]**, QINWEI GUO**[3]**, ZHONGSHI ZHANG**[4]**,
AZIGULI WULAMU[1,5]**, AND DEZHENG ZHANG**[1,5]

[1]School of Computer and Communication Engineering, University of Science and Technology Beijing, Beijing 100083, China
[2]Surgical Simulation Research Laboratory, Department of Surgery, University of Alberta, Edmonton, AB T6G 2E1, Canada
[3]Institute of Sports Medicine, Peking University Third Hospital, Beijing 100191, China
[4]Department of Biological Sciences, University of Alberta, Edmonton, AB T6G 2E9, Canada
[5]Beijing Key Laboratory of Knowledge Engineering for Materials Science, Beijing 100083, China

Corresponding authors: Bin Zheng (bin.zheng@ualberta.ca) and Qinwei Guo (guoqinwei@vip.sina.com)

ABSTRACT Deep learning has been applied in healthcare, where features of patients are read by the computer to assist with diagnosis and treatment. In sports medicine, kinematic characteristics of injuries need to be defined. Patients' data are then acquired amplified to training deep learning models. In this study, we tracked motions of lower extremities in patients with lateral collateral ligament injuries of the ankle. Key kinematic characteristics of injuries were identified by comparing patients to normal individuals. The deep convolutional generative adversarial networks (DCGANs) was employed to synthesize a modest-sized labeled dataset to avoid the problems raised from using large-scale manual labeling data. We then fed a combination of real and synthesized data to train long short-term memory (LSTM) networks to detect patients with ligament injuries. The results showed that combined data yielded a better outcome, measured by classification accuracy and f1-score, than solely using the patient data or with a large quantity of synthesized single range of motion feature.

INDEX TERMS Kinematic characteristics, lateral collateral ligament injuries (LCL injuries) of the ankle, injuries detection, deep convolutional generative adversarial networks (DCGANs), long short-term memory (LSTM) networks.

I. INTRODUCTION

Kinematics-based intelligent diagnosis is a crucial technique to improve precision medicine in sports injuries [1] [2]. As an important weight-bearing joint in the lower extremity, ankle is the most vulnerable joint in the human body [3]. The lateral collateral ligament injuries (LCL injuries) of the ankle are particularly common because the lateral ligaments are weaker than the medial [4]. The incidence of LCL injuries of the ankle was one case per 10,000 person-day in the world, ranking first in trauma emergency cases [5]. There is an urgent need to develop an intelligent diagnosis method for

the patients with LCL injuries of the ankle, which can detect the injuries automatically, accurately, and immediately either in the acute phase or during rehabilitation [6], [7].

Deep learning provides a convenient possible solution for intelligent diagnosis, but the medical dataset in training restricts the practical application [8], [9]. Because it is paramount to protect patient privacy, accessing large datasets is often restricted within medical and healthcare institutions. Furthermore, the large-scale manual labeling of medical datasets from the unstructured fashion leads to considerable variability in standards [10].

The size of training sets directly impacts on the detection performance in deep learning [11]. Generative adversarial networks (GANs) proposed by Goodfellow expanded the

The associate editor coordinating the review of this manuscript and approving it for publication was Donato Impedovo.

training data by unsupervised learning [12]. GANs provides a new solution for the problem that medical data is not enough in model training [13]. Alec Radford *et al.* proposed the deep convolutional generative adversarial networks (DCGANs), combining the GANs and the convolutional neural network [14]. DCGANs explore the potential pattern from complex data and generate high-quality synthesized samples, supplementing the training sets for intelligent detections [15]. There were many pieces of pilot research using DCGANs, such as aging face generation, Parkinson's voiceprint samples augment, computerized tomography image reconstruction, skin lesion classification, and liver lesion classification [16]–[20].

In this paper, we first measured the foot and ankle kinematic characteristics of LCL injuries of the ankle using the Heidelberg Foot Measurement Method (HFMM). Once we identified the key kinematic characteristics of LCL injuries, we employed the DCGANs to synthesize features of those injuries, then data were taken in the long short-term memory (LSTM) networks to automatically detect patients with LCL injuries. As a means of augmenting datasets under controlled conditions, the generative networks, trained by the injury and control group independently, simulated the probability distribution of kinematic characteristics in walking. The synthesized features increased the quality and quantity of labeled samples for training the detection model. We used the Pearson correlation coefficient method and t-distribution Stochastic Neighbor Embedding (t-SNE) algorithm to evaluate the relevance between the real and synthesized features and trained the LSTM networks by real and synthesized features for the LCL injuries of the ankle detection.

II. RELATED WORK
A. FOOT AND ANKLE KINEMATICS
To detect the LCL injuries, it is important to look for the difference between normal and injured foot and ankle motion throughout each gait cycle. The model assumption of the foot as a single rigid segment in previous studies is no longer acceptable. Recent studies for objectively measuring the static and kinematic characteristics of the foot and ankle using multi-segment foot models are reported. Kim *et al.* compared ankle joint kinematics as well as ligament and muscle strains using two-segment, three-segment, and five-segment foot models during vertical hopping. The study showed that the model covering all foot structures was superior to the talus into one segment in ankle joint biomechanics [21].

Preliminary works in sports medicine have built several multi-segment foot models and applied these motion-tracking metrics to measure gait behaviors. Canseco *et al.* provided a quantitative characterization of gait kinematics in patients with hallux rigidus using the Milwaukee Foot Model (MFM), a four-segment foot model introduced by Canseco *et al.* [22], Kidder *et al.* [23]. The marker-based segmental definition of foot included the tibia, hindfoot, forefoot, and hallux. Balsdon *et al.* investigated the between-day reliability and

within-session variability of the Oxford Foot Model (OFM), a multi-segment rigid model developed at the Oxford Gait Laboratory [24]. The OFM based on two main foot segments (hindfoot and forefoot) plus a separate hallux segment has been used clinically on patients with cerebral palsy, club foot, toe walkers, and other foot-related question [25]. Nicola *et al.* modified the Rizzoli Foot Model (RFM), a five-segment rigid model described by Leardini *et al.*, to describe the foot and ankle motion of teenagers with pes-planus [26], [27]. This five-segment model included the shank, foot overall, calcaneus, mid-foot, and metatarsus. Wouter *et al.* compared the kinematic output of the OFM and RFM during normal gait and typical pathological gait patterns in healthy adults. The results revealed that the OFM measured a larger range of motion (ROM) in the hindfoot-shank joint, but the RFM measured a larger ROM in the forefoot-hindfoot joint. The differences between these two models were significantly in equinus and toe-out gait [28]. From this study, we are reminded that careful consideration is warranted when measuring the gait kinematics using a multi-segment foot model.

Simon *et al.* developed a kinematic measurement protocol, HFMM, to measure foot function including almost all typical foot deformities for clinical practice [29]. The marker-based segmental definition covered the shank, hindfoot, midfoot, and the forefoot. The HFMM identified angular definitions to describe the multi-segmental motion of the foot and ankle and developed a reliable marker set for the shank and all foot. The reliability and validity of these measurement methods have been tested in walking on a level surface in people with no-known abnormalities and patients with hallux rigidus before/after cheilectomy, low arched feet, or Charcot-Marie-Tooth disease, *et al.* [30]–[32].

B. GENERATIVE ADVERSARIAL NETWORKS IN GAIT RECOGNITION
A considerable volume of kinematic data will certainly help with the intelligent detection for LCL injuries of the ankle. However, data annotation is time-consuming, the data from each subject required hours for surgical experts in labeling those gait kinematics recorded. It is uncommon that deep learning algorithms run on data with relatively small volumes. The GANs help us make up this gap synthesizing and augmenting data. Currently, GANs have been initially introduced to the field of gait recognition for data synthesis.

1) USING MICRO-DOPPLER SPECTROGRAMS
Doherty *et al.* presented a GANs-trained unsupervised model using micro-Doppler spectrograms for gait detection [33]. Abdulatif *et al.* used GANs to learn the joint distribution of the training data for denoising and reconstructing the micro-Doppler spectrograms in human walking [34]. Erol *et al.* proposed multi-branch GANs integrating the kinematic analysis of the micro-Doppler signature envelope to generate abnormal gait samples [35]. The results showed that there was greater overlap between the synthesized and real abnormal gait samples in the feature space.

2) USING GAIT IMAGES

Babaee *et al.* used GANs to reconstruct gait energy images for addressing the problem of gait recognition from an incomplete gait cycle. This approach was evaluated on the OULP large gait dataset to confirm that the GANs-based synthesis architecture was efficient [36]. He *et al.* proposed multi-task GANs for learning view-specific feature representations with period energy images. The multi-task GANs extended more discriminative features from gait sequences for cross-view gait recognition. The competitive performance has been shown on OU-ISIR, CASIA-B, and USF benchmark datasets [37]. Li *et al.* presented the cycle-consistent attentive GANs to map different views' gait images to view-consistent and photorealistic images for cross-view gait recognition. The experimental results demonstrate that the synthesized data help the gait recognition model get better outcomes [38]. Furthermore, there were serval superior GANs, such as Gait GANs [39], RGB GANs [40], view transformation GANs [41], variation normalizing GANs[42], and parallel GANs [43], for image-based gait features augmentation and reconstruction.

There are few works for foot and ankle kinematic characteristics augmentation using GANs at present. However, kinematics is crucial for clinical reasoning in sports medicine. With the development of the motion-tracking technologies, the kinematic measure has serval precisely quantified studies in foot and ankle behaviors for clinic practice. This study connects the intelligent technologies to kinematics synthesizing foot and ankle kinematic characteristics for automatic LCL injuries detection.

III. FOOT AND ANKLE KINEMATIC CHARACTERISTICS

A. DATA ACQUISITION

We placed 17 reflective markers (13 of 9 mm, 4 of 14 mm reflective markers) on each side of the lower extremity below the knee to track foot and ankle motions. The markers were stuck on the key bony landmarks. The three-dimensional (3D) perspective of the lower extremity in Vicon Nexus is shown in Fig. 1A. The markers' placement followed the HFMM [29], [31].

The motion data was captured by the Vicon MX Motion Capture System (Lucent Technologies Inc.) with eight MX Cameras. The motion capture system used infrared emission cameras to illuminate reflective markers and recorded their 3D coordinate data at 100 Hz.

Each subject was required to walking in barefoot along a 10 meters flat path at his comfortable speed (Fig. 1B). The raw position data for each subject were exported as.csv files from Vicon Nexus 1.8.5 for future analysis.

B. PRE-PROCESSING

The raw position data were filtered by a low-pass zero phase shift first-order Butterworth filter with no more than 1dB of ripple in passband from 0 to 0.01Hz, and at least 3dB of attenuation in the stopband above 20Hz to reduce the
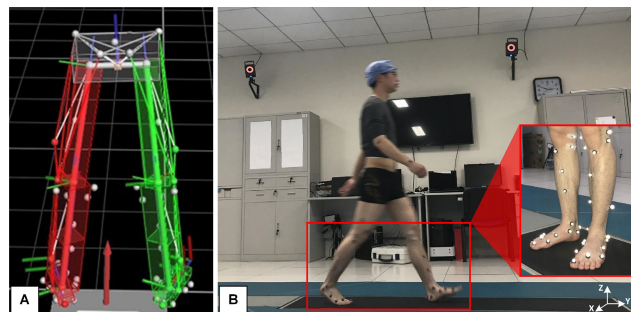

FIGURE 1. (A) 3D perspective of the low extremity in Vicon Nexus; (B) Motion tracking by Vicon MX Motion Capture System. Note: the captured position data are mapped into a fixed 3D coordinate system aligned with the lab area.

noise from the environment, marker shift, and other uncertain factors [44].

The gait in natural walking is periodic. An intact gait cycle includes a stance phase (from heel-strike to toe-off) and a swing phase (from toe-off to heel-strike again) [45]. The marker CCL is placed in the most prominent part of the dorsal calcaneus. At heel-strike, the position of CCL at the Z-axis reaches a minimal value. This moment is defined as the ending of the last gait cycle and the beginning of a new gait cycle (Fig. 2). To make data comparable among subjects, we normalized each gait cycle to 100 sample points by linear interpolation.
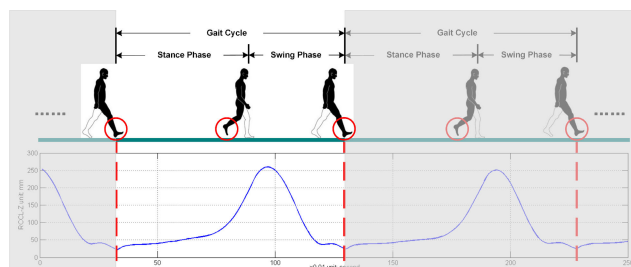

FIGURE 2. Segmenting method of gait cycles. Bold line is the CCL position at the Z-axis; dashed is the heel-strike moment.

C. KINEMATICS MEASURE

The range of motion (ROM) profiles were calculated by seven angle features and a distance feature (Fig. 3), including tibiotalar flexion (A), forefoot/ankle abduction (B), medial arch angle (C), lateral arch angle (D), subtalar rotation (E), forefoot/ankle supination (F), MT I-V angle (G), and lateral malleolus scale (H). These HFMM-based features were largely independent of each other and were considered clinically relevant as the revealing pathologic features of the gait after LCL injuries of the ankle. The description of these features is shown in Table 1 [29].

D. NORMALIZATION

To improve the convergence speed and accuracy of the deep learning model (DCGANs and LSTM), we normalized each
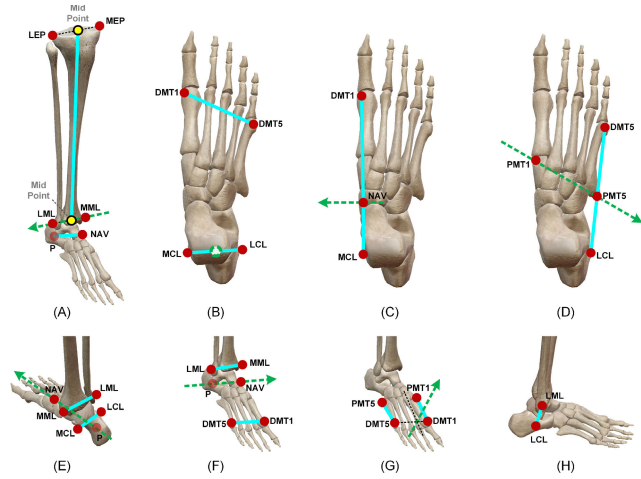
FIGURE 3. HFMM-based kinematics measure. (A) tibiotalar flexion; (B) forefoot/ankle abduction; (C) medial arch angle; (D) lateral arch angle; (E) subtalar rotation; (F) forefoot/ankle supination; (G) MT I–V angle; (H) lateral malleolus scale. LEP/MEP: lateral/medial epicondyle; LML/MML: lateral/medial malleolus; LCL/CCL/MCL: lateral/dorsal/medial calcaneus; NAV: navicular; PMT1/PMT5: proximal end of 1st/5th metatarsal; DMT1/DMT5: distal end of 1st/5th metatarsal.

TABLE 1. Description of ROM features.

No.	ROM Feature	Marker	Description
A	tibiotalar flexion	LEP/MEP LML/MML LCL/CCL/ MCL	Flexion between Tibia and Talus around Ankle (close to the sagittal plane).
B	forefoot/ ankle abduction	LML/MML DMT1/5	Rotation between Forefoot and Ankle around the axis vertical upward (close to transverse plane).
C	medial arch angle	MCL NAV DMT1	Angle between the line from NAV to DMT1 and the line from NAV to MCL around the axis perpendicular to these two lines (close to the sagittal plane).
D	lateral arch angle	LCL PMT1/5 DMT5	Angle between the line from PMT5 to DMT5 and the line from LCL to PMT5 around Midfoot (close to the sagittal plane).
E	subtalar rotation	LML/MML LCL/CCL/ MCL	Rotation between Calcaneus and Ankle around Talus (close to the frontal plane).
F	forefoot/ ankle supination	LML/MML LML/CCL/ MCL DMT1/DM T5	Angle between Forefoot and Ankle around Talus (close to the frontal plane).
G	MT I–V angle	NAV DMT1/5 PMT1/5	Angle between the line from PMT1 to DMT1 and the line from PMT5 to DMT5 around the line perpendicular to the line from Midfoot Center to Forefoot Center and Forefoot (close to transverse plane).
H	lateral malleolus scale	LML/LCL	Distance between LML and LCL.

Note: Tibia: line from knee joint center (midpoint between LEP and MEP) to ankle joint center (midpoint between LML and MML); **Talus:** line from point P (P=(2LCL+MCL+CCL)/4) to NAV marker; **Ankle:** line from MML to LML; **Calcaneus:** line from MCL to LCL; **Midfoot:** line from PMT1 to PMT5; **Forefoot:** line from DMT1 to DMT5; **Midfoot Center:** center of NAV, PMT1, and PMT5; **Forefoot Center:** (3*DMT1+2*DMT5)/5.

value of ROM features to the range of 0 to 1 [24]. The feature's normalization is defined as

$$f^* = \frac{f - f_{min}}{f_{max} - f_{min}} \qquad (1)$$

where f^* is the normalized feature, f is the feature before normalization, f_{max} is the feature's maximum value in the training set, and f_{min} is the feature's minimum value in the training set.

IV. SYNTHESIZING MODEL AND ASSESSMENT

The proposed method had two stages as shown in Fig. 4A. The first stage trained DCGANs using a dataset of labeled ROM features to learn the distribution of real data. The second stage used this trained generator to synthesize new features. The DCGANs were trained for the injury and control group independently, so the labels of synthesized features is known. The synthesized and real features trained the LSTM-based LCL injuries detection model together as shown in Fig. 4B.

A. SYNTHESIZING KINEMATIC CHARACTERISTICS

GANs is an unsupervised machine learning and is composed of two neural networks: a generator and a discriminator. The adversarial competition between generator and discriminator improves the networks' performance [46]. The DCGANs synthesizing kinematic characteristics used fractionally-strided convolutions and strided convolutions to replace the pooling layers in generator and discriminator, respectively.

The generator G builds a potential probability distribution P_g of training data for real kinematic characteristics and proposes a mapping $G(z, \theta_g)$ from the input noise variable $p_z(z)$, where θ_g is the set of learning parameters of the deep

convolutional neural network in the generator [47]. As shown in Fig. 4A, the input of the generator is a 100-dimensional noise vector z depending on uniform distribution between -1 and 1. The noise z is projected and reshaped to spatial convolutional representation with 512 feature maps. A series of four fractionally-strided convolutions convert 1×50 feature maps into ROM features $\hat{F}_{1 \times 800}$.

The discriminator network $D(x, \theta_d)$ receives synthesized features $\hat{F}$ and real features F and then produces an output to declare the input features are real or synthesized after passing the four convolution layers.

The generator aims to generate random samples as real ROM features. While the discriminator tries to distinguish between the synthesized and real features. Therefore, DCGANs training is a minimax process [48]. The discriminator maximizes the loss value, while the generator tries to minimize it [49]. The adversarial competition between the
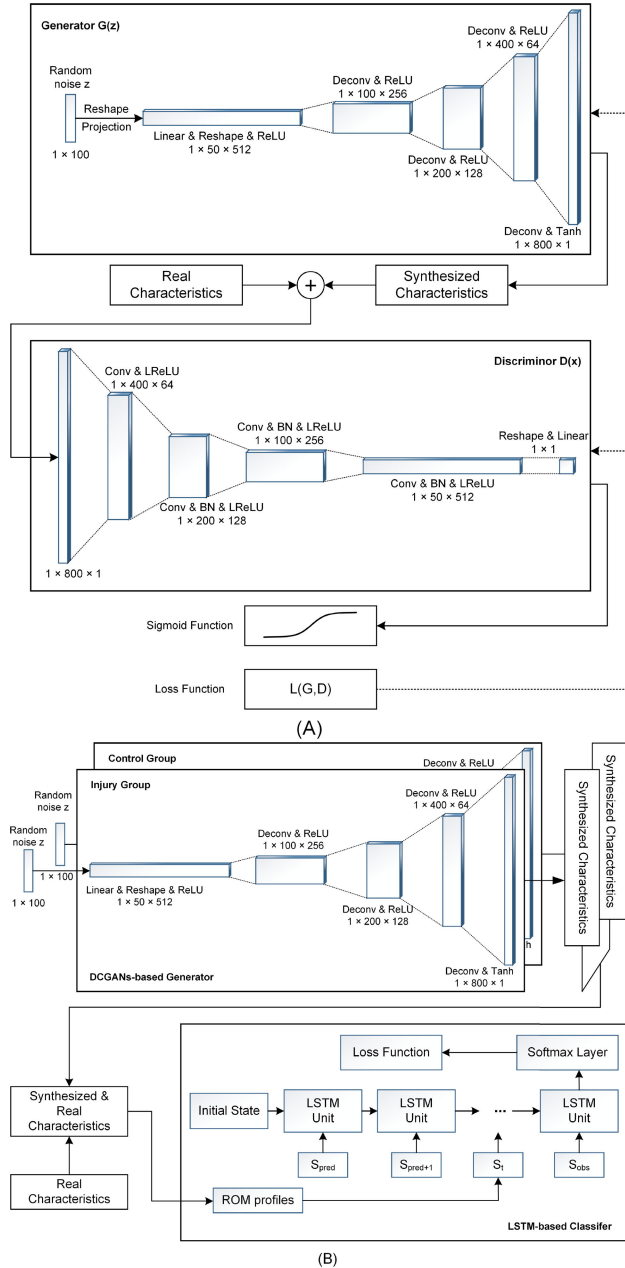
FIGURE 4. System design of the proposed method. (A) Thearchitecture of the DCGANs and training it with real kinematic characteristics. The model is trained for the injury group and control group independently. (B) Top: Synthesizing kinematic characteristics using trained generators for each. Bottom: Architecture of the LSTM networks and training it with real and synthesized kinematic characteristics to detect LCL injuries of the ankle.

generator and discriminator is indicated as

$$\min_{G} \max_{D} L\,(D, G) = \mathbb{E}_{x \sim P_{data}(x)}\,[log D\,(x)]$$
$$+\mathbb{E}_{z \sim P_z(z)}[log(1 - D\,(G(z)))] \quad (2)$$

where, $\mathbb{E}_{x \sim P_{data}(x)}$ and $\mathbb{E}_{z \sim P_z(z)}$ are the expectation from the real and synthesized features; $D\,(x) \in [0, 1]$ is the probability that the sample x is deemed to be real; $D\,(G(z)) \in [0, 1]$ is the probability that the synthesized feature $G(z)$ is deemed to be real.

The independently trained generator by the control and injury group is used to synthesize kinematic characteristics as shown in Fig. 4B. The shuffled concatenation of real and synthesized kinematic characteristics is fed to the LSTM networks for LCL injuries detection.

Fig. 5 shows a series of randomly selected synthesized kinematic characteristics at different learning epochs of DCGANs and a group of real characteristics. The first epoch (Epoch0) started with the initialization of DCGANs parameters. After 2500 epochs, we can observe a fuzzy structure of kinematic characteristics as shown in Fig. 5 (Epoch2500). After 5000 and 7500 epochs, a trend-consistent structure of the characteristics is becoming visible. In epoch 10000, further details such as the stance and swing phase in a gait cycle, adjustment amplitude between frames become coordinated.
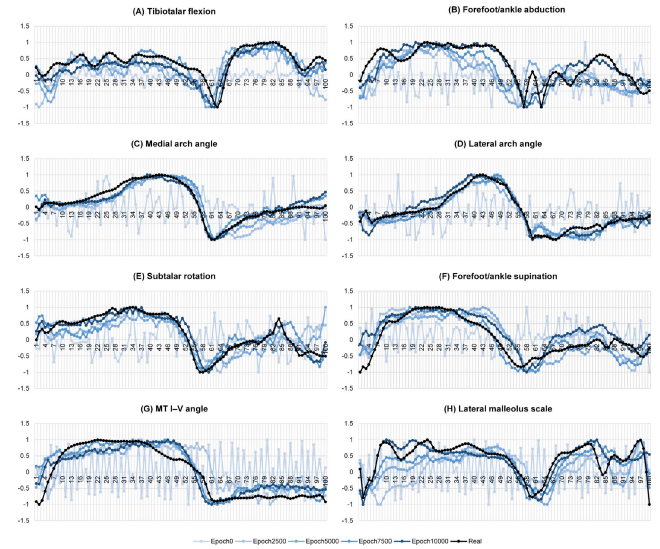

FIGURE 5. Randomly selected a set of synthesized features for injury group at different training epochs of the DCGANs. The real features from a patient with LCL injuries of the ankle.

B. ASSESSMENT FOR SYNTHESIZED CHARACTERISTICS

It is challenging to measure the quality of synthesized features versus real features frame by frame because the synthesized features do not belong to a real fixed pattern. We used the Pearson correlation coefficient and the t-SNE algorithm to compare the similarity of synthesized features to the real.

1) PEARSON CORRELATION COEFFICIENT

Pearson correlation coefficient $\rho_{\hat{F},F}$ is used to evaluate the linear correlation between synthesized ROM features $\hat{F}(\hat{f}_1, \hat{f}_2, \ldots, \hat{f}_8)$ and the real $F(f_1, f_2, \ldots, f_8)$ [50]. The Person correlation coefficient is calculated as

$$\rho_{\hat{F},F} = \frac{cov(\hat{F}, F)}{\sigma_{\hat{F}} \sigma_F} = \frac{E\left(\left(\hat{F} - \mu_{\hat{F}}\right)(F - \mu_F)\right)}{\sigma_{\hat{F}} \sigma_F}$$
$$= \frac{E\left(\hat{F}F\right) - E\left(\hat{F}\right)E(F)}{\sqrt{E\left(\hat{F}^2\right) - E^2(\hat{F})}\sqrt{E\left(F^2\right) - E^2(F)}} \quad (3)$$

where σ is the standard deviation, $cov(\cdot)$ is the covariance between synthesized features $\hat{F}$ and the real F, E is the mathematical expectation, μ is mean value.

When $\rho_{\hat{F},F}$ is in $(0.8, 1.0]$, the degree of correlation between the synthesized features $\hat{F}$ and the real F is very strong. When $\rho_{\hat{F},F}$ is in $(0.6, 0.8]$, the degree of correlation is strong. When $\rho_{\hat{F},F}$ is in $(0.4, 0.6]$, the degree of correlation is medium. When $\rho_{\hat{F},F}$ is in $(0.2, 0.4]$, the degree of correlation is weak. When $\rho_{\hat{F},F}$ is in $[0.0, 0.2]$, the degree of correlation is very weak or no correlation.

2) VISUALIZATION USING T-SNE

The visual verification for synthesized features by the t-SNE algorithm consists of two stages [51]. First, t-SNE constructs a probability distribution over pairs of high-dimensional features in such a way that the probability of being picked is proportional to the similarity of objects. Second, t-SNE defines a similar probability distribution over the features in the low-dimensional map for visualization. The details are as follows [52].

The Euclidean distance in high-dimensional space is transformed into a conditional probability. Give a set of n high-dimensional features (shuffled concatenation of real and synthesized) $f_1, f_2, \ldots, f_n$, the conditional probability $p_{j|i}$ of features f_j and f_i is defined as

$$p_{j|i} = \frac{\exp(-\| f_i - f_j \|^2 / 2\sigma_i^2)}{\sum_{m \neq i} \exp(-\| f_i - f_m \|^2 / 2\sigma_i^2)} \quad (4)$$

where σ_i searched by the binary search algorithm is a variance of the Gaussian distribution centered at f_i.

The similarity in high-dimensional features is defined as a symmetrized version of the conditional probability, that is:

$$p_{ij} = \frac{p_{j|i} + p_{i|j}}{2n} \quad (5)$$

To reflect the similarity p_{ij} in the low-dimensional map as well as possible, the similarity between two features f'_i and f'_j in the map is defined as

$$q_{ij} = \frac{(1 + \| f'_i - f'_j \|^2)^{-1}}{\sum_{m \neq i}(1 + \| f'_i - f'_m \|^2)^{-1}}, q_{ii} = 0 \quad (6)$$

The location of the features f'_i in the low-dimensional map is determined by minimizing the Kullback-Leiber divergence between the probability distribution $P = (p_{ij})$ and $Q = (q_{ij})$ using the gradient descent algorithm, that is:

$$KL(P \parallel Q) = \sum_{i \neq j} p_{ij} \log \frac{p_{ij}}{q_{ij}} \quad (7)$$

$$\frac{\delta KL(P \parallel Q)}{\delta f'_i} = 4 \sum_j (p_{ij} - q_{ij})(f'_i - f'_j)(1 + \| f'_i - f'_j \|^2)^{-1} \quad (8)$$

The result of this algorithm is a map that describes the high-dimensional ROM features in a low-dimensional space to verify the synthesizing quality from visualization.

V. EXPERIMENTS

A. DATA

This is an interdisciplinary study done at several institutes in Canada and China. The protocol was reviewed and approved by the Institutional Research Board of Peking University Third Hospital where data collected were executed. Each participant provided written consent before they enrolled in the study.

The injured gait data captured from three patients diagnosed with LCL injuries of the ankle before surgery (all-male, the average age of 34). Five healthy adults with paired age and gender were recruited from the student and staff of the hospital and university to serve as control subjects (all-male, the average age of 25). The true human kinematics dataset consisted of 86 normal gait cycles and 30 injury gait cycles. The training set for the synthesizing model included 50 gait cycles from three control subjects and 20 gait cycles from two patients. The remaining data from another two healthy subjects and one patient differing from the training set was used for testing.

We created three different strategies for feeding data to train the detection model and compared their outcomes. The first feeding strategy (DFS1), as same as the training set for the synthesizing model, only included real ROM features. The second feeding strategy (DFS2) included the real features plus 200 synthesized features for each group. The third feeding strategy (DFS3) included the real features plus 1000 synthesized features for each group.

B. TECHNICAL DETAILS OF TRAINING AND IMPLEMENTATION

1) SYNTHESIZING MODEL

The DCGANs model was trained independently for the injury and control groups. The injury group used a batch size of 16, and the control group used a batch size of 32. The number of training epochs was set to 10,000. The learning rate for Adam optimizer was 0.002 and the momentum term was 0.5. The prior input noise variable $p_z(z)$ was a 100-dimensional vector with continuous uniform distribution randomly synthesized values in $[-1, 1]$. The initial weights of DCGANs were set by a Gaussian distribution with zero mean and 0.02 standard deviation.

The generator consisted of a fully connected layer and 4 deconvolution layers with 5×5 kernel size and 2 stride size. Batch-normalization (BN) was applied to each hidden layer. The fully connected layer in the generator reshaped the input into size $1 \times 50 \times 512$. The output of each fractional-strided convolution layer expanded to twice its input size. The generator's output layer used the tanh activation function and the hidden layers used the ReLU activation function.

The discriminator consisted of a fully connected layer and 4 convolution layers with 5×5 kernel size and 2 stride size. BN was applied to each hidden layer. The hidden layers used the Leaky ReLU activation function after BN and the output layer used the sigmoid activation function.

TABLE 2. Pearson correlation coefficient of 5 randomly selected samples for each group.

	Sample	Tibiotalar flexion (A)	Forefoot/ankle abduction (B)	Medial arch angle (C)	Lateral arch angle (D)	Subtalar rotation (E)	Forefoot/ankle supination (F)	MT I-V angle (G)	Lateral malleolus scale (H)
injury group	1	0.81	0.70	0.95	0.81	0.81	0.87	0.94	0.81
	2	0.72	0.71	0.95	0.92	0.78	0.86	0.97	0.92
	3	0.71	0.78	0.94	0.97	0.80	0.81	0.96	0.97
	4	0.89	0.84	0.90	0.96	0.85	0.82	0.93	0.96
	5	0.72	0.88	0.98	0.96	0.82	0.86	0.94	0.96
	Avg.	0.77	0.78	0.94	0.92	0.81	0.84	0.95	0.92
control group	1	0.87	0.78	0.84	0.93	0.79	0.95	0.99	0.82
	2	0.89	0.92	0.90	0.96	0.76	0.84	0.96	0.88
	3	0.95	0.86	0.82	0.94	0.84	0.84	0.95	0.81
	4	0.98	0.77	0.92	0.94	0.82	0.86	0.97	0.68
	5	0.91	0.93	0.84	0.96	0.65	0.90	0.96	0.81
	Avg.	0.92	0.85	0.87	0.95	0.77	0.88	0.96	0.80

2) DETECTION MODEL

LSTM is a powerful computer algorithm for performing classification work on the entire time series [53]. The LSTM detection model in this study included an input layer, two hidden layers, and a Softmax classifier as the output layer. There were 32 memory units for each hidden layer. The stochastic gradient descent (SGD) algorithm was used for the model training. Using the Root Mean Square Prop (RMSProp) algorithm was to reduce the swing amplitude during parameter optimizing and accelerate the rate of convergence [54]. The categorical cross-entropy loss function was added after the Softmax classifier to estimate the level of inconsistency between the prediction and true value. The number of training iterations was set to 300 and the batch size was 32. According to the three DFSs, we designed two kinds of detection experiments: 1) detecting the LCL injuries through each ROM features independently (the input was batches of 1×100 feature vectors); 2) detecting the LCL injuries through eight ROM features together (the input was batches of 1×800 feature vectors). There were two diagnostic tags (0 and 1) for the detection model output. Tag 0 represented the normal and tag 1 represented the LCL injuries of the ankle.

C. VALIDATION FOR SYNTHESIZED CHARACTERISTICS
1) CORRELATION ANALYSIS

We randomly selected 5 samples from real and synthesized data for each group and paired off. The Pearson correlation coefficients of eight ROM features for each pair were calculated respectively as shown in Table 2. The correlation coefficients were above 0.65 for every pair and the average of 5 samples' correlation coefficients were all above 0.77 for each ROM feature. It means that there was a strong linear correlation between the real and synthesized features.

The synthesized features were consistent with the real, but they were not identical.

2) VISUAL VERIFICATION

The eight ROM features in gait cycles were mapped into a plane respectively using the t-SNE algorithm (perplexity was set to 30). Fig. 6 shows the visualization of real and 200 randomly selected synthesized ROM features. The synthesized ROM features overlapped with the same class of real ROM features and generalized within their certain range. The synthesized features of forefoot/ankle abduction (B) and lateral malleolus scale (H) had a sharp border for each class. The synthesized features of tibiotalar flexion (A), media arch angle (C), and forefoot/ankle supination (F) had bits of overlapping features while the real data are more distinguished. The features of subtalar rotation (E) and MT I-V angle (G) were closer to each other. This observation might be due to the subtle differences between LCL injuries of the ankle and control groups with less visible features to the human eye.

D. INJURIES DETECTION

We calculated accuracy, precision, recall, and f1-score based on the confusion matrix to measure the effect for the detection with three different training sets. Accuracy defined as $ACC = (TP + TN) / (TP + TN + FP + FN)$ is a measure of the classification performance of a detection model. Here, TP is the number of true predictions for the normal, TN is the number of true predictions for the LCL injuries, FP is the number of false predictions for the normal, FN is the number of false predictions for the LCL injuries. Precision-Recall is used to measure the success of prediction [55]. Precision is defined as $P = TP / (TP + FP)$. Recall is defined
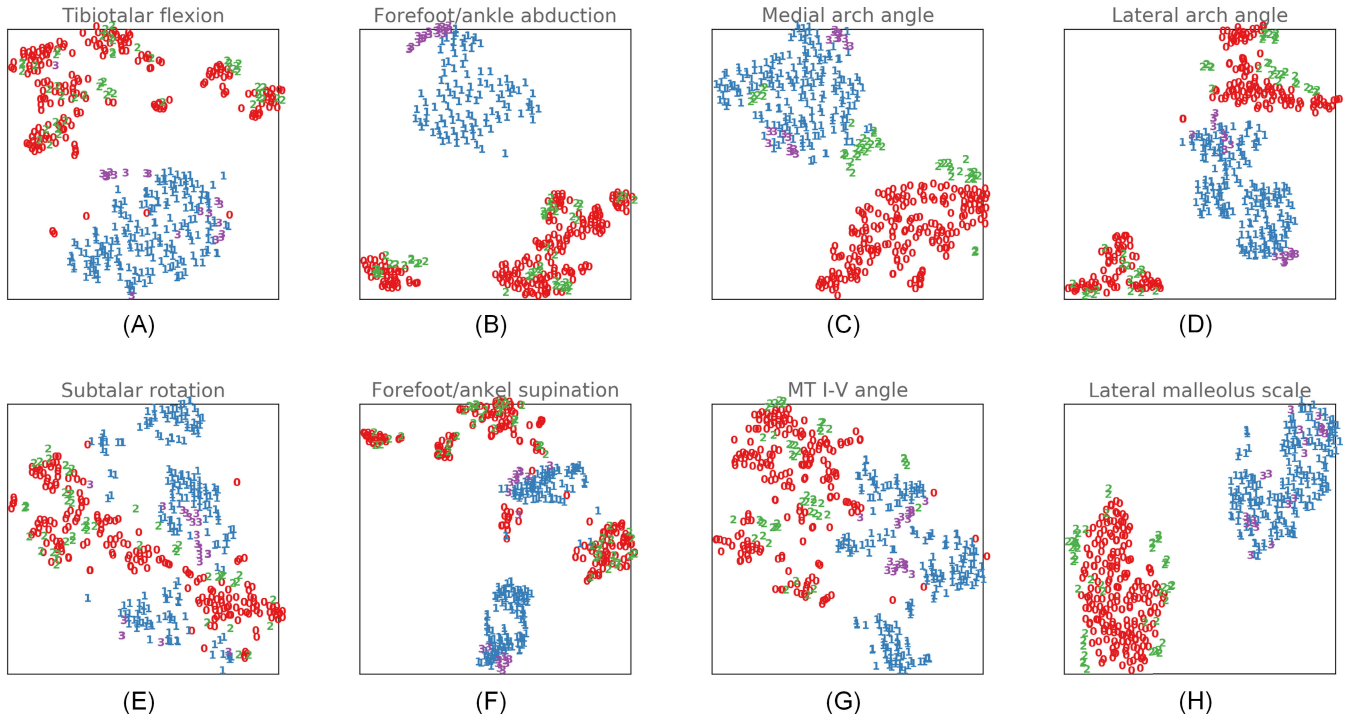
FIGURE 6. Visualization of real and synthesized gait kinematics using the t-SNE algorithm. Digit 0 (red color) in the chart represents 200 randomly selected synthesized ROM features for the control group; digit 1 (blue color) in the chart represents 200 randomly selected synthesized ROM features for the injury group; digit 2 (green color) in the chart represents 50 real ROM features for the control group; digit 3 (purple color) in the chart represents 20 real ROM features for the injury group.

TABLE 3. Accuracy, precision, recall, and f1-score for LCL injuries detection using a single ROM feature for three DFSs on the same test dataset.

DFS	Measure	Tibiotalar flexion (A)	Forefoot/ankle abduction (B)	Medial arch angle (C)	Lateral arch angle (D)	Subtalar rotation (E)	Forefoot/ankle supination (F)	MT I-V angle (G)	Lateral malleolus scale (H)	Avg.
DFS1	accuracy (%)	84.78	73.91	67.39	71.74	78.26	71.74	50.00	91.30	73.64
	precision	1.00	1.00	1.00	0.77	0.78	0.85	1.00	1.00	0.93
	recall	0.81	0.67	0.58	0.92	1.00	0.78	0.36	0.88	0.75
	f1-score	0.89	0.80	0.74	0.84	0.88	0.81	0.53	0.94	0.80
DFS2	accuracy (%)	93.48	84.78	65.22	56.52	91.30	71.74	65.22	91.30	77.45
	precision	1.00	0.97	1.00	0.75	1.00	0.93	0.75	1.00	0.93
	recall	0.91	0.83	0.56	0.67	0.89	0.69	0.83	0.89	0.78
	f1-score	0.96	0.90	0.71	0.71	0.94	0.79	0.79	0.94	0.84
DFS3	accuracy (%)	93.48	93.48	78.26	71.74	76.09	76.09	67.39	89.13	80.71
	precision	1.00	0.97	0.78	0.87	1.00	1.00	0.96	1.00	0.95
	recall	0.92	0.94	1.00	0.75	0.69	0.69	0.61	0.86	0.81
	f1-score	0.96	0.96	0.88	0.81	0.82	0.82	0.75	0.93	0.87

as $R = TP/(TP + FN)$. f_1 defined as $f_1 = (2 \cdot P \cdot R)/(P + R)$ is the harmonic mean of precision and recall.

The accuracy, precision, recall, and f1-score for LCL injuries detection using a single ROM feature are presented in Table 3. The training set for the detection model only using real features (DFS1) did not yield adequate classification outcomes. The accuracy for the

tibiotalar flexion, forefoot/ankle abduction, medial arch angle, lateral arch angle, subtalar rotation, and forefoot/ankle supination (A-F) were moderated (about $67\% \sim 85\%$); the accuracy for MT I-V angle (G) was a random guess (50.00%); the accuracy for lateral malleolus (H) scale was satisfied (91.30%). The average accuracy for all the features was moderated (73.64%). The average accuracy improved slightly (77.45%) when 200 synthesized features were added
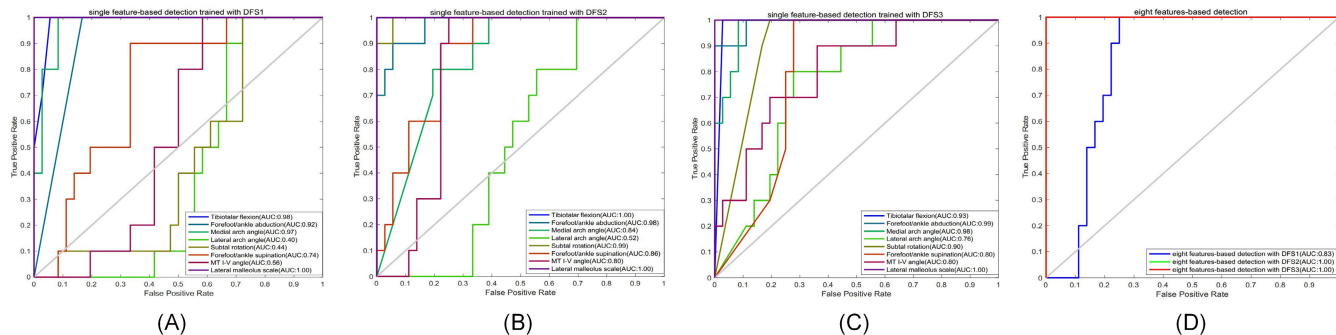
FIGURE 7. ROC curves for detecting LCL injuries of the ankle. (A) single feature-based detection trained with DFS1; (B) single feature-based detection trained with DFS2; (C) single feature-based detection trained with DFS3; (D) eight features-based detection.

to the training set. The average accuracy improved dramatically (80.71%) adding 1000 synthesized features to train the detection model. On this training condition (DFS3), the improvement of accuracy for the tibiotalar flexion, forefoot/ankle abduction, medial arch angle, forefoot/ankle supination, and MT I-V angle (A-C, F, G) were satisfied. It is acceptable that the accuracy for lateral arch angle (D) remained constant (71.41%) and the accuracy for subtalar rotation (E) and lateral malleolus scale (H) decreased slightly (E: from 78.26% to 76.09%; H: from 91.30% to 89.13%). Adding 200 synthesized features to the training set can improve the f1-score for half of the features (A, B, E, G). Compared to the DFS1, the average of the f1-scores for eight features improved slightly with DFS2 (from 0.80 to 0.84). Adding 1000 synthesized features to the training set can improve the trade-off between precision and recall for most of the ROM features (A-C, F-H). The average of f1-score with DFS3 was higher than with DFS2 (0.87 vs. 0.84). The f1-scores show that the detection model had a poor performance in the classification of forefoot/ankle abduction (B), medial arch angle (C), and MT I-V angle (G) using DFS1. Using 1000 synthesized features as the training set promoted their f1-score dramatically. Our results showed that the importance of features for the classification with a ranking is the tibiotalar flexion (A) and forefoot/ankle abduction (B) > the medial arch angle (C) and lateral malleolus scale (H) > the subtalar rotation (E) and forefoot/ankle supination (F) > the lateral arch angle (D) and MT I-V angle (G). By the way, the visualization using the t-SNE algorithm in Fig. 6 already provided some insights.

Although the detection accuracy for each feature was spotty, all the eight ROM features made substantial contributions in their single feature-based LCL injuries detection. We integrated these features for training the detection model. We tested the detection with the three DFSs for five times, the accuracy, precision, recall, f1-score, and specificity for the test with medium results are shown in Table 4. Training with real features (DFS1) did not yield adequate detection outcomes. The accuracy, precision, recall, and f1-score were moderated, and the specificity is low. When we added 200 synthesized features, the outcome was

TABLE 4. Accuracy, precision, recall, f1-score, and specificity for LCL injuries detection using eight ROM features for three DFSS on the same test dataset.

DFS	accuracy	precision	recall	f1-score	specificity
DFS1	73.91%	0.77	0.94	0.85	0.00
DFS2	97.83%	1.00	0.97	0.99	1.00
DFS3	100.00%	1.00	1.00	1.00	1.00

dramatically improved. With increasing the sample size by adding 1000 synthesized features to the training set, the outcomes further improved. The acceptable option was the real plus 1000 synthesized ROM features, where the accuracy, precision, recall, f1-score, and specificity were all satisfied.

The receiver operating characteristic (ROC) plots in Fig. 7(A-C) also show that adding synthesized ROM features to the training set improved the trade-off between true positive rate and false positive rate. In the case of detection by a single kind of ROM feature, adding 1000 synthesized features to the training sets generally was better than adding 200. The detection accuracy was further improved by eight ROM features together (Fig. 7D).

VI. CONCLUSION

We report our works in detecting patients with LCL injuries using a deep learning methodology. When ligaments surrounding patients' foot and ankle get injured, patients' mobilization will be disturbed. In this study, we quantitatively described the behavior surrounding foot and ankle in natural walking based on data collected by HFMM. Noticing the true human data was insufficient for deep learning, we used DCGANs to synthesize data with the eight ROM features for the injuries. We have shown that synthesized ROM features can augment the training dataset, resulting in a substantial improvement in both single feature-based and eight feature-based LCL injuries detection performance. We obtained the best results with a combination of true human and 1000 synthesized features in training the LSTM networks for classification.

The quality of synthesized features was evaluated using the Pearson correlation coefficient and the t-SNE algorithm.

The results from calculating the Pearson correlation coefficient show that there was a strong linear correlation between the real and synthesized features for each class. The visualization using the t-SNE algorithm shows that the synthesized ROM features were closed to their real counterparts per class.

Our experiment results also show that augmenting datasets with synthesized ROM features can improve the diversity of the dataset to enhance the generalization performance of the detection model. The size of the training dataset is a direct factor impacting on the detection performance for LCL injuries. Therefore, the moderate training set can improve the classification and generation performance for the LCL injuries detection model reducing the misdiagnosis and missed diagnosis rate.

Our long-term goal is to develop an artificial intelligence-based instrument for automatically detecting the LCL injuries of the ankle. This study focuses on one aspect of patients' behaviors (i.e. range of motion) that connects to their foot and ankle kinematic characteristics during walking. Current research proves the feasibility of using the synthesizing model for LCL injuries detection. This is only a small but concrete step toward our long-term goal. By closely working with surgeons, we will extend our research to inspect more specific behaviors around micro-adjustment of foot and ankle in gait, posture control in different sports situations, sequentially optimize our detection model, and eventually enhance the quality of clinical assessment of human movement in sports medicine.

REFERENCES

[1] Z. S. Wang, W. M. Chen, and D. J. Wang, "A new diagnosis tool for knee osteoarthritis based on lower-limb kinematics model combined with muscle activity analysis," *Basic Clin. Pharmacol.*, vol. 126, pp. 14–15, Apr. 2020.

[2] J. J. Kim, H. Cho, Y. Park, J. Jang, J. W. Kim, and J. S. Ryu, "Biomechanical influences of gait patterns on knee joint: Kinematic & EMG analysis," *PLoS ONE*, vol. 15, no. 5, May 2020, Art. no. e0233593, doi: 10.1371/journal.pone.0233593.

[3] G. Moisan, C. Mainville, M. Descarreaux, and V. Cantin, "Kinematic, kinetic and electromyographic differences between young adults with and without chronic ankle instability during walking," *J. Electromyogr. Kinesiol.*, vol. 51, Apr. 2020, Art. no. 102399, doi: 10.1016/j.jelekin.2020.102399.

[4] M. H. Leonard, "Injuries of the lateral ligaments of the ankle: A clinical and experimental study," *J. Bone Joint Surg. Amer.*, vol. 31, no. 2, pp. 373–377, 1949, doi: 10.2106/00004623-194931020-00013.

[5] M. Lacko, Z. Sidor, S. Stolfa, R. Cellar, and G. Vasko, "Acute injuries of lateral ankle joint ligaments," *Rozhledy v Chirurgii*, vol. 89, no. 7, pp. 461–465, Aug. 2010. [Online]. Available: https://www.ncbi.nlm.nih.gov/pubmed/20925265

[6] S. Qiu, L. Liu, Z. Wang, S. Li, H. Zhao, J. Wang, J. Li, and K. Tang, "Body sensor network-based gait quality assessment for clinical decision-support via multi-sensor fusion," *IEEE Access*, vol. 7, pp. 59884–59894, 2019.

[7] I. Ud Din, A. Almogren, M. Guizani, and M. Zuair, "A decade of Internet of Things: Analysis in the light of healthcare applications," *IEEE Access*, vol. 7, pp. 89967–89979, 2019.

[8] H. Salehinejad, E. Colak, T. Dowdell, J. Barfett, and S. Valaee, "Synthesizing chest X-ray pathology for training deep convolutional neural networks," *IEEE Trans. Med. Imag.*, vol. 38, no. 5, pp. 1197–1206, May 2019, doi: 10.1109/Tmi.2018.2881415.

[9] L. Wang, Y. Sun, Q. Li, T. Liu, and J. Yi, "Two shank-mounted IMUs-based gait analysis and classification for neurological disease patients," *IEEE Robot. Autom. Lett.*, vol. 5, no. 2, pp. 1970–1976, Apr. 2020, doi: 10.1109/Lra.2020.2970656.

[10] D. Pinto dos Santos, S. Brodehl, B. Baeßler, G. Arnhold, T. Dratsch, S.-H. Chon, P. Mildenberger, and F. Jungmann, "Structured report data can be used to develop deep learning algorithms: A proof of concept in ankle radiographs," *Insights Imag.*, vol. 10, no. 1, Sep. 2019, doi: 10.1186/s13244-019-0777-8.

[11] F. J. Gonzalez, H. F. Satizabal, A. Perez-Uribe, and J. A. Lopez, "DCGAN model used to generate body gestures on a human-humanoid interaction system," in *Proc. IEEE Colombian Conf. Appl. Comput. Intell. (ColCACI)*, Jun. 2019, pp. 1–5.

[12] I. J. Goodfellow, "Generative adversarial nets," in *Proc. Adv. Neural Inf. Process. Syst. (NIPS)*, vol. 27, 2014, pp. 2672–2680.

[13] T. Salimans, I. Goodfellow, W. Zaremba, V. Cheung, A. Radford, and X. Chen, "Improved techniques for training GANs," in *Proc. Adv. Neural Inf. Process. Syst. (NIPS)*, vol. 29, 2016, pp. 2234–2242.

[14] A. Radford, L. Metz, and S. Chintala, "Unsupervised representation learning with deep convolutional generative adversarial networks," 2015, *arXiv:1511.06434*. [Online]. Available: http://arxiv.org/abs/1511.06434

[15] G. Zheng, G. Han, N. Q. Soomro, L. Ma, F. Zhang, Y. Zhao, X. Zhao, and C. Zhou, "A novel computer-aided diagnosis scheme on small annotated set: G2C-CAD," *BioMed Res. Int.*, vol. 2019, Apr. 2019, Art. no. 6425963, doi: 10.1155/2019/6425963.

[16] X. Liu, Y. Zou, C. Xie, H. Kuang, and X. Ma, "Bidirectional face aging synthesis based on improved deep convolutional generative adversarial networks," *Information*, vol. 10, no. 2, p. 69, Feb. 2019, doi: 10.3390/info10020069.

[17] R. A. Zanini and E. L. Colombini, "Parkinson's disease EMG data augmentation and simulation with DCGANs and style transfer," *Sensors*, vol. 20, no. 9, p. 2605, May 2020, doi: 10.3390/s20092605.

[18] A. Ben-Cohen, E. Klang, S. P. Raskin, S. Soffer, S. Ben-Haim, E. Konen, M. M. Amitai, and H. Greenspan, "Cross-modality synthesis from CT to PET using FCN and GAN networks for improved automated lesion detection," *Eng. Appl. Artif. Intell.*, vol. 78, pp. 186–194, Feb. 2019, doi: 10.1016/j.engappai.2018.11.013.

[19] F. Pollastri, F. Bolelli, R. Paredes, and C. Grana, "Augmenting data with GANs to segment melanoma skin lesions," *Multimedia Tools Appl.*, vol. 79, nos. 21–22, pp. 15575–15592, Jun. 2020, doi: 10.1007/s11042-019-7717-y.

[20] M. Frid-Adar, I. Diamant, E. Klang, M. Amitai, J. Goldberger, and H. Greenspan, "GAN-based synthetic medical image augmentation for increased CNN performance in liver lesion classification," *Neurocomputing*, vol. 321, pp. 321–331, Dec. 2018, doi: 10.1016/j.neucom.2018.09.013.

[21] H. Kim and K. Kipp, "Number of segments within musculoskeletal foot models influences ankle kinematics and strains of ligaments and muscles," *J. Orthopaedic Res.*, vol. 37, no. 10, pp. 2231–2240, Oct. 2019, doi: 10.1002/jor.24394.

[22] K. Canseco, J. Long, R. Marks, M. Khazzam, and G. Harris, "Quantitative characterization of gait kinematics in patients with hallux rigidus using the Milwaukee foot model," *J. Orthopaedic Res.*, vol. 26, no. 4, pp. 419–427, Jan. 2008, doi: 10.1002/jor.20506.

[23] S. M. Kidder, F. S. Abuzzahab, G. F. Harris, and J. E. Johnson, "A system for the analysis of foot and ankle kinematics during gait," *IEEE Trans. Rehabil. Eng.*, vol. 4, no. 1, pp. 25–32, Mar. 1996, doi: 10.1109/86.486054.

[24] M. E. R. Balsdon and C. E. Dombroski, "Reliability of a multi-segment foot model in a neutral cushioning shoe during treadmill walking," *J. Foot Ankle Res.*, vol. 11, no. 1, p. 60, Dec. 2018, doi: 10.1186/s13047-018-0301-2.

[25] P. C. Dixon, J. Stebbins, T. Theologis, and A. B. Zavatsky, "Ground reaction forces and lower-limb joint kinetics of turning gait in typically developing children," *J. Biomech.*, vol. 47, no. 15, pp. 3726–3733, Nov. 2014, doi: 10.1016/j.jbiomech.2014.09.011.

[26] A. Leardini, M. G. Benedetti, L. Berti, D. Bettinelli, R. Nativo, and S. Giannini, "Rear-foot, mid-foot and fore-foot motion during the stance phase of gait," *Gait Posture*, vol. 25, no. 3, pp. 453–462, Mar. 2007, doi: 10.1016/j.gaitpost.2006.05.017.

[27] N. Portinaro, A. Leardini, A. Panou, V. Monzani, and P. Caravaggi, "Modifying the Rizzoli foot model to improve the diagnosis of pes-planus: application to kinematics of feet in teenagers," *J. Foot Ankle Res.*, vol. 7, no. 1, p. 57, Dec. 2014, doi: 10.1186/s13047-014-0057-2.

[28] W. Schallig, J. C. van den Noort, J. McCahill, J. Stebbins, A. Leardini, M. Maas, J. Harlaar, and M. M. van der Krogt, "Comparing the kinematic output of the Oxford and Rizzoli foot models during normal gait and voluntary pathological gait in healthy adults," *Gait Posture*, vol. 82, pp. 126–132, Oct. 2020, doi: 10.1016/j.gaitpost.2020.08.126.

[29] J. Simon, L. Doederlein, A. S. McIntosh, D. Metaxiotis, H. G. Bock, and S. I. Wolf, "The Heidelberg foot measurement method: development, description and assessment," *Gait Posture*, vol. 23, no. 4, pp. 411–424, Jun. 2006, doi: 10.1016/j.gaitpost.2005.07.003.

[30] B. Kuni, S. I. Wolf, F. Zeifang, and M. Thomsen, "Foot kinematics in walking on a level surface and on stairs in patients with hallux Rigidus before and after cheilectomy," *J. Foot Ankle Res.*, vol. 7, no. 1, p. 13, Dec. 2014, doi: 10.1186/1757-1146-7-13.

[31] D. Twomey, A. S. McIntosh, J. Simon, K. Lowe, and S. I. Wolf, "Kinematic differences between normal and low arched feet in children using the Heidelberg foot measurement method," *Gait Posture*, vol. 32, no. 1, pp. 1–5, May 2010, doi: 10.1016/j.gaitpost.2010.01.021.

[32] T. Dreher, S. I. Wolf, D. Heitzmann, C. Fremd, M. C. Klotz, and W. Wenz, "Tibialis posterior tendon transfer corrects the foot drop component of cavovarus foot deformity in Charcot-Marie-Tooth disease," *J. Bone Joint Surgery*, vol. 96, no. 6, pp. 456–462, Mar. 2014, doi: 10.2106/jbjs.l.01749.

[33] H. G. Doherty, L. Cifola, R. I. A. Harmanny, and F. Fioranelli, "Unsupervised learning using generative adversarial networks on micro-doppler spectrograms," in *Proc. 16th Eur. Radar Conf. (EuRAD)*, Oct. 2019, pp. 197–200.

[34] S. Abdulatif, K. Armanious, F. Aziz, U. Schneider, and B. Yang, "Towards adversarial denoising of radar micro-Doppler signatures," in *Proc. Int. Radar Conf. (RADAR)*, Sep. 2019, pp. 1–6, doi: 10.1109/RADAR41533.2019.171396.

[35] B. Erol, S. Z. Gurbuz, and M. G. Amin, "Synthesis of micro-Doppler signatures for abnormal gait using multi-branch discriminator with embedded kinematics," in *Proc. IEEE Int. Radar Conf. (RADAR)*, Apr. 2020, pp. 175–179.

[36] M. Babaee, Y. Zhu, O. Kopuklu, S. Hormann, and G. Rigoll, "Gait energy image restoration using generative adversarial networks," in *Proc. IEEE Int. Conf. Image Process. (ICIP)*, Sep. 2019, pp. 2596–2600, doi: 10.1109/ICIP.2019.8803236.

[37] Y. He, J. Zhang, H. Shan, and L. Wang, "Multi-task GANs for view-specific feature learning in gait recognition," *IEEE Trans. Inf. Forensics Security*, vol. 14, no. 1, pp. 102–113, Jan. 2019, doi: 10.1109/TIFS.2018.2844819.

[38] S. Li, W. Liu, H. Ma, and S. Zhu, "Beyond view transformation: cycle-consistent global and partial perception gan for view-invariant gait recognition," in *Proc. IEEE Int. Conf. Multimedia Expo (ICME)*, Jul. 2018, pp. 1–6, doi: 10.1109/ICME.2018.8486484.

[39] S. Yu, H. Chen, E. B. G. Reyes, and N. Poh, "GaitGAN: Invariant gait feature extraction using generative adversarial networks," in *Proc. IEEE Conf. Comput. Vis. Pattern Recognit. Workshops (CVPRW)*, Jul. 2017, pp. 532–539, doi: 10.1109/CVPRW.2017.80.

[40] N.-D.-T. Tieu, H. H. Nguyen, F. Fang, J. Yamagishi, and I. Echizen, "An RGB gait anonymization model for low-quality silhouettes," in *Proc. Asia–Pacific Signal Inf. Process. Assoc. Annu. Summit Conf. (APSIPA ASC)*, Nov. 2019, pp. 1686–1693, doi: 10.1109/APSIPAASC47483.2019.9023188.

[41] P. Zhang, Q. Wu, and J. Xu, "VT-GAN: View transformation GAN for gait recognition across views," in *Proc. Int. Joint Conf. Neural Netw. (IJCNN)*, Jul. 2019, pp. 1–8, doi: 10.1109/IJCNN.2019.8852258.

[42] P. Zhang, Q. Wu, and J. Xu, "VN-GAN: identity-preserved variation normalizing GAN for gait recognition," in *Proc. Int. Joint Conf. Neural Netw. (IJCNN)*, Jul. 2019, pp. 1–8, doi: 10.1109/IJCNN.2019.8852401.

[43] X. Li, Y. Makihara, C. Xu, Y. Yagi, and M. Ren, "Make the bag disappear: Carrying status-invariant gait-based human age estimation using parallel generative adversarial networks," in *Proc. IEEE 10th Int. Conf. Biometrics Theory, Appl. Syst. (BTAS)*, Sep. 2019, pp. 1–9, doi: 10.1109/BTAS46853.2019.9185973.

[44] J. Sinclair, P. J. Taylor, and S. J. Hobbs, "Digital filtering of three-dimensional lower extremity kinematics: An assessment," *J. Hum. Kinetics*, vol. 39, no. 1, pp. 25–36, Dec. 2013, doi: 10.2478/hukin-2013-0065.

[45] T. Ito, A. Tsubahara, Y. Shiraga, Y. Yoshimura, D. Kimura, K. Suzuki, and K. Hanayama, "Motor activation is modulated by visual experience during cyclic gait observation: A Transcranial magnetic stimulation study," *PLoS ONE*, vol. 15, no. 1, Jan. 2020, Art. no. e0228389, doi: 10.1371/journal.pone.0228389.

[46] W. Fang, Y. Ding, F. Zhang, and J. Sheng, "Gesture recognition based on CNN and DCGAN for calculation and text output," *IEEE Access*, vol. 7, pp. 28230–28237, 2019, doi: 10.1109/ACCESS.2019.2901930.

[47] T. Fujioka, M. Mori, K. Kubota, Y. Kikuchi, L. Katsuta, M. Adachi, G. Oda, T. Nakagawa, Y. Kitazume, and U. Tateishi, "Breast ultrasound image synthesis using deep convolutional generative adversarial networks," *Diagnostics*, vol. 9, no. 4, p. 176, Nov. 2019, doi: 10.3390/diagnostics9040176.

[48] A. Diaz-Pinto, A. Colomer, V. Naranjo, S. Morales, Y. Xu, and A. F. Frangi, "Retinal image synthesis and semi-supervised learning for glaucoma assessment," *IEEE Trans. Med. Imag.*, vol. 38, no. 9, pp. 2211–2218, Sep. 2019, doi: 10.1109/Tmi.2019.2903434.

[49] T. Fujioka, K. Kubota, M. Mori, L. Katsuta, Y. Kikuchi, K. Kimura, M. Kimura, M. Adachi, G. Oda, T. Nakagawa, Y. Kitazume, and U. Tateishi, "Virtual interpolation images of tumor development and growth on breast ultrasound image synthesis with deep convolutional generative adversarial networks," *J. Ultrasound Med.*, early access, Jun. 17, 2020, doi: 10.1002/jum.15376.

[50] J. L. Turner, "The parametric Pearson's product moment correlation coefficient statistic," in *ESL Appl Linguist*. New York, NY, USA: Routledge, 2014, pp. 275–299.

[51] L. Hajderanj, I. Weheliye, and D. Chen, "A new supervised t-SNE with dissimilarity measure for effective data visualization and classification," in *Proc. 8th Int. Conf. Softw. Inf. Eng. (ICSIE)*, 2019, pp. 232–236, doi: 10.1145/3328833.3328853.

[52] H. Kang, J.-S. Park, K. Cho, and D.-Y. Kang, "Visual and quantitative evaluation of amyloid brain PET image synthesis with generative adversarial network," *Appl. Sci.*, vol. 10, no. 7, p. 2628, Apr. 2020, doi: 10.3390/app10072628.

[53] S. Hochreiter and J. Schmidhuber, "Long short-term memory," *Neural Comput.*, vol. 9, no. 8, pp. 1735–1780, Nov. 1997, doi: 10.1162/neco.1997.9.8.1735.

[54] D. Liang, F. Ma, and W. Li, "New gradient-weighted adaptive gradient methods with dynamic constraints," *IEEE Access*, vol. 8, pp. 110929–110942, 2020, doi: 10.1109/Access.2020.3002590.

[55] J. Davis and M. Goadrich, "The relationship between precision-recall and ROC curves," in *Proc. 23rd Int. Conf. Mach. Learn. (ICML)*, Pittsburgh, PA, USA, Jun. 2006, pp. 233–240.

XIN LIU received the B.E. degree in electronic information engineering and the Ph.D. degree in control science and engineering from the University of Science and Technology Beijing, China, in 2009 and 2015, respectively. From 2015 to 2017, she held a postdoctoral position in information and communication systems. Since 2017, she has been an Assistant Professor and a M.E. Supervisor with the Computer Science and Technology Department, School of Computer and Communication Engineering, University of Science and Technology Beijing. From 2019 to 2020, she was a Visiting Scholar with the Department of Surgery, University of Alberta. Her research interests include high-level data analysis, intelligent information processing, data mining, and decision making in medicine.

CHEN ZHAO received the B.E. degree from Qufu Normal University, Rizhao, China, in 2019. She is currently pursuing the M.E. degree in computer technology with the University of Science and Technology Beijing, Beijing, China. Her research interests include machine learning in medicine data processing and computer-aided injuries detection.

BIN ZHENG received the M.D. and M.S. degrees in medicine, China, and the Ph.D. degree in kinesiology from Simon Fraser University, Canada. Differing from most medical researches focusing on patients, he put healthcare providers under the spotlight. Explicitly, he studies the performance and cognition of physicians and surgeons during surgery, especially in image-guided and robotic surgery, such as endoscopic and laparoscopic surgery. He is currently an Associate Professor in surgery and the Endowed Research Chair in surgical simulation with the Department of Surgery, University of Alberta. He has collaborates with surgeons, engineers, clinical educators, and psychologists to develop the artificial intelligence and simulation programs for training surgeons.

AZIGULI WULAMU received the Ph.D. degree in control theory and its applications from the University of Science and Technology Beijing, Beijing, China, in 2004. She was a Visiting Scholar with the Technische Universität Kaiserslautern, Germany, from August 2001 to October 2002. She is currently a Professor and a Ph.D. Supervisor with the School of Computer and Communication Engineering, University of Science and Technology Beijing. Her research interests include knowledge engineering, knowledge graph, deep learning, and artificial intelligence technologies.

QINWEI GUO received the M.D. degree in sports medicine from the Peking University Health Science Center, Beijing, China, in 2002. In 2002, he held a Sports Medicine Surgeon position with the Peking University Third Hospital, where he has been an Associate Professor and a Chief Physician with the Institute of Sports Medicine, since 2011. His research interests include sports injury, ligament reconstruction of ankle and knee, articular cartilage repair, and arthroscopy.

DEZHENG ZHANG received the Ph.D. degree in control theory and its applications from the University of Science and Technology Beijing, Beijing, China, in 2002. He is currently a Professor and a Ph.D. Supervisor with the School of Computer and Communication Engineering, University of Science and Technology Beijing. He is also the Director of the Beijing Key Laboratory of Knowledge Engineering for Materials Science. His current research interests include big data mining, artificial intelligence technologies, and knowledge engineering.

ZHONGSHI ZHANG is currently pursuing the B.S. degree in biological sciences with the University of Alberta, Edmonton, AB, Canada. He was a Summer Student with the Surgical Simulation Research Laboratory, University of Alberta. His research interests include medicine data analysis and processing.

• • •